ELSEVIER

Neutron scattering, electron microscopy and dynamic mechanical studies of carbon nanofiber/phenolic resin composites

Mitra Yoonessi[a],*, Hossein Toghiani[b], Robert Wheeler[c], Lionel Porcar[d,e], Steve Kline[d], Charles U. Pittman Jr.[f]

[a]Department of Chemical Engineering, University of New Hampshire, NH 03824, United States
[b]Dave C. Swalm School of Chemical Engineering, Mississippi State, MS 39762, United States
[c]Wright Patterson Air Force Research Laboratory, WPAFB, OH 45433, United States
[d]NIST Center for Neutron Research, National Institute of Standards and Technology, Gaithersburg, MD 20899, United States
[e]University of Maryland College Park, United States
[f]Department of Chemistry, Mississippi State University, Mississippi State, MS 39762, United States

ARTICLE INFO

ABSTRACT

Carbon nanofiber (CNF)/resole phenolic resin (Hitco 134A) composites exhibited very large increases of bending storage modulus above the glass transition temperature and had higher glass transition temperatures with increasing CNF weight percentage. Small angle neutron scattering (SANS) from dilute suspensions of surface-oxidized CNF in D_2O exhibited a Guinier plateau in the q range examined, indicating that isolated scatterers exist. The CNF dispersion, average fiber diameter, average core diameter and polydispersity within the composites and in D_2O were quantified by approximating the small angle neutron scattering data with a hollow tube model. The scattering from CNF/phenolic resin composites exhibited a q^{-4} power law behavior, indicating the presence of sharp interfaces between fibers and phenolic resin. Surface-oxidized (PR-19-PS) CNF nanocomposites exhibited lower surface to volume ratio values and larger shell thickness compared with heat-treated (PR-19-HT) CNF composites. However, carbon nanofibers, with and without oxygenated surface groups, exhibited some agglomerates with fractal dimensions within the phenolic resin composites. Fiber surface treatment with nitric acid appears to promote dispersion and results in looser bundles of nested fiber networks.

1. Introduction

The discovery of carbon nanofibers [1,2] promoted many studies of their applications including catalyst supports for direct methanol fuel cells [3], hydrogen storage media [4], remotely-actuated shape-memory characteristics [5,6], composite reinforcements [7,8], electromagnetic shielding, [9] and highly conductive coatings [10]. The extraordinary enhancements in polymer/CNF composite thermal and mechanical properties [7,8] as well as electrical properties [10] and electromagnetic shielding [9,10] are due to the large tensile moduli [11] and high thermal and electrical conductivities of CNFs [12]. The final properties of CNF composites are dictated by the inherent properties, interfacial characteristics, three-dimensional orientation and morphology of the fibers. Overcoming the attractive forces causing formation of fiber aggregates, disentangling

fiber nests, controlling polymer fiber interactions and promoting dispersion and CNF orientation have been major challenges to achieve optimized properties both in thermoset and thermoplastic resins. High (30–50)% by weight loadings of CNF in resole phenolic resin exhibited remarkable high temperature erosion resistances in plasma torch tests at 1650 °C, potentially providing new materials for rocket nozzle applications [13] and solid propellant rocket motor liners [14,15]. CNF phenolic resin composites have also been examined as precursors for carbon–carbon composites [16].

Thermal and mechanical properties of composites are impacted by the fibers' modulus, stiffness, thermal and electrical conductivities and also by the fiber dispersion and three-dimensional orientation in the polymer matrix. Carbon nanofibers have strong tendency to agglomerate, due to strong attractive fiber van der Waals forces. They form nest-like entanglements due to their curvature and high aspect ratios. The extent of disagglomeration and dispersion both in liquids and in resins depends on the relative van der Waals forces (for carbon nanofibers), curvature and on the relative surface energy of CNFs versus that of the solvent or resin. Mechanical energy and intense ultrasonication have frequently been used to overcome attractive forces, but some rebundling of the aggregates can occur after discontinuation of the external force. Surface modifications can improve the CNF dispersion. Plasma [17–19] and acid treatments [20] generate surface functionality that improves dispersion. Surface grafting to improve distribution in thermoplastics has been reported [15–17]. Despite the critical role that dispersion plays, the effect of the CNF size, geometry and extent of dispersion in resin composites has not been well understood.

We now report large improvements in dynamic storage bending moduli above T_g for carbon nanofiber/phenolic resin composites with small weight percentages of CNFs. For the first time, some in-situ geometrical characteristics of CNFs within cured phenolic resins have been analyzed. A modified polydisperse hollow tube model and a generalized unified fractal model [21] were utilized to provide an understanding of the small angle neutron scattering (SANS) from CNF in the composites and in dilute water dispersions. Attempts were made to correlate the fiber characteristics and dispersion with thermal and mechanical properties.

2. Experimental

2.1. Sample preparation

A resole phenolic resin (Fig. 1), Hitco 134A containing 30–40 wt.% isopropyl alcohol and amine components (Hitco Carbon Composites, Inc.), D_2O, 99.9 atom% D, and tetrahydrofuran (THF) (Aldrich Chemical Co.) were used without further purification. A Resole phenolic resin is composed of a variety of monomeric, dimeric, and trimeric hydroxylmethylated phenols (Fig. 1). Pyrograph III carbon nanofiber PR-19-HT (without treatment) and PR-19-PS (Applied Sciences Inc.) (after acid treatments) were used. Highly graphitized PR-19-HT fiber had been heat-treated to 2800–3000 °C during the fiber synthesis. PR-19-PS, a pyrolitically stripped fiber with larger diameters, was treated with 60% by weight nitric acid
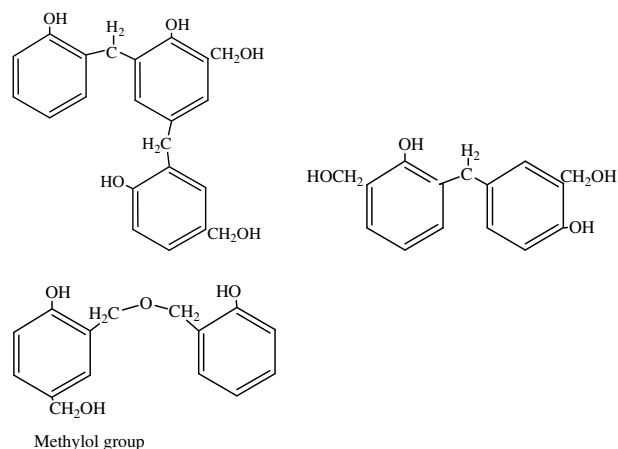

Fig. 1 – Resole phenolic resin molecular structure.

at 115 °C for 1 h to generate surface ester, anhydride, quinoid, and phenolic hydroxyl functions [20]. These fibers contain highly preferred graphitic hexagonal basal planes which can lie from almost parallel to the normal axis of the fiber to a cant angle ~25°. These inner filament structures (Dixie cup morphology) can be thickened by a turbostratic CVD-deposited outer layer as the residence time increases [22–25]. Heat-treated 2800–3000 °C carbon fibers are highly graphitized and have smaller average diameters 50–200 nm. Presence of amorphous carbon at the canted edges provides the possibility of surface oxidation.

PR-19-PS fibers were oxidized in refluxing 60–70% by weight HNO_3 as described in our earlier work [20]. This fiber was dispersed in D_2O by sonicating for 10 min (ultrasonic processor Model GE501, Ace Glass, 20 KHz, 500 W). Phenolic resin/(1–4)% by weight CNF composites were prepared by dispersing CNF in THF, sonicating for 30 min and then mixing with 40% by weight phenolic resin THF solutions. These dispersions were sonicated for another 30 min to further disperse the fibers and wet the CNF surfaces with phenolic components followed by solvent removal in a vacuum oven (10 mbar) for 17 h at 70 °C. Partial phenolic resin pre-curing also occurred, locking the CNF in place and preventing reaggregation. The pre-cured phenolic resin/CNF was then cooled to room temperature and powdered by a mixer/crusher. The CNF/phenolic resin pre-cured powder was then placed in a steel mold and cured in a hot press at 88 °C for 45 min, followed by 149 °C for 5 h.

2.2. Characterization methods

2.2.1. SANS measurements

Ultra high resolution small angle and small angle neutron scattering (USANS and SANS, respectively) experiments were performed at the National Institute of Standards and Technology (NIST), Center for Neutron Research (NCNR) using the 30 m NG-7 SANS instrument and the BT5 perfect-crystal diffractometer. For the SANS measurements, a cold neutron wavelength of $\lambda = 6$ Å ($\Delta\lambda/\lambda = 10\%$) and sample to detector positions of 1, 4 and 15 m ($\lambda = 8$ Å) were used ($10^{-3} < q(\text{Å}^{-1}) < 0.3$). Scattered intensities were reduced and corrected for the transmission, background and parasitic

scattering using Igor Pro® version 5.0 (WaveMetrics, Inc.) and software supplied by NIST [26]. The scattered intensities were then circularly averaged to produce a one-dimensional graph of scattering intensity, $I(q)$, as a function of the wave vector, q, where $q = (4\pi/\lambda)\sin(\theta/2)$ and θ is the scattering angle [26]. USANS experiments covered a q-range of $0.00005 < q$ (Å^{-1}) < 0.01, corresponding to a real-space length scale of 0.1–10 μm [27,28].

2.2.2. Modeling of scattered intensities

The coherent scattering intensity, $I(q)$, from a concentrated dispersion is defined as the product of the form factor, $P(q)$, the structure factor, $S(q)$ and the instrumental constant k.

$$I(q) = kP(q) \cdot S(q) \tag{1}$$

$P(q)$ is related to the scattered wave amplitude arising from the particle shape and the structure factor is due to particle–particle interactions. The structure factor is equal to one for a dilute dispersion ($S(q) = 1$). Therefore, the scattering from a non-interacting particle suspension is proportional to the particle form factor. The form factor for a hollow cylinder, Fig. 2, is defined as a function of cylinder volume, V_{cyl}, scattering length density (SLD) of the solvent, $\rho_{solv.}$ and the scattering length density of the cylinder shell, ρ_1 (Eq. (2)). The polydispersity in radius has been taken into consideration using a log-normal distribution (Eqs. (3) and (4)), where the length and the shell thickness are monodisperse [29–32]. The angle of the cap was negligible:

$$P(q) = \int_0^{\pi/2} \sin\theta \cdot \left[V_1(\rho_1 - \rho_{sol}) \frac{\sin\left(\frac{qH_1 \cos\theta}{2}\right)}{\frac{qH_1 \cos\theta}{2}} \frac{2J_1(qR_1 \sin\theta)}{qR_1 \sin\theta} \right.$$
$$\left. + V_P(\rho_P - \rho_1) \frac{\sin\left(\frac{qH_P \cos\theta}{2}\right)}{\frac{qH_P \cos\theta}{2}} \frac{2J_1(qR_P \sin\theta)}{qR_P \sin\theta} \right]^2 d\theta \tag{2}$$

$$I(q) = \frac{1}{V_P} \sum_{R_P} n(R_P, \sigma_P) P(q, R_P, R_1, H_P, H_1, \rho_P, \rho_1, \rho_{solv.}) \tag{3}$$

$$n(R_P) = \frac{\exp\left(-\frac{1}{2}\left[\frac{\ln(R_P/R_0)}{\sigma_P}\right]^2\right)}{\sqrt{2\pi}\sigma_P R_P} \tag{4}$$

$$V_x = \pi R_x^2 H_x \tag{5}$$

The cylinder form factor is averaged over all orientations, where theta is the angle between the cylinder axis and the scattering wave vector, q. $J_1(x)$ is the first order Bessel function,
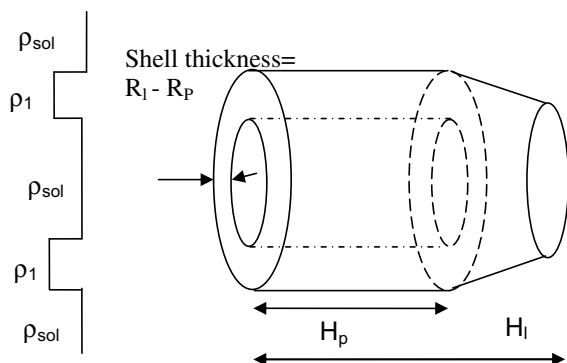
R_P is the core radius, H_P is the core length. The mean core radius is R_0, with a standard deviation of the Gaussian distribution, σ_P. The face shell thickness and fiber radius is obtained by $H_1 = H_P + 2^*$ face thickness and $R_1 = R_P +$ radial thickness.

This model can be simplified to a cylinder form factor where R_1 is the fiber radius and H_1 is the fiber length. The contrast term is the difference between SLD of medium ($\rho_{solv.}$) and SLD of fiber (ρ_1).

The radius of gyration for a system of non-interacting particles can be obtained from a Guinier approximation to the low q data when $qR_g \leqslant 1$ [29,30].

$$I(q) = I_0 \exp(-q^2 R_g^2/3) \tag{6}$$

Here, I_0 is the intensity at $q = 0$ and R_g is the radius of gyration.

A two-step unified exponential/power law (Beaucage model) describes the CNF morphology and structure of fractals [21]. This model assumes that scattering results from fractal objects in several length scales. Therefore, predicting these length scales by the unified model can describe fibers' radius of gyration and also provide information regarding nesting and aggregates structure in the low q regime. Each structural level is described by a radius of gyration at low q and a power law slope at higher q.

$$I(q) = \sum_{i=1}^N G_i \exp(-q^2 R_{g,i}/3) + \frac{B_i[\text{erf}]qR_{g,i}/\sqrt{6}]^{3P_i}}{q^{P_i}} \tag{7}$$

The scattered intensity was compared with Beaucage's unified model (Eq. (7), $N = 2$) to extract R_g, the power law exponents, P, the Guinier prefactors, G, and the power law prefactor, B, associated with each length scale.

2.2.3. Transmission electron microscopy

High resolution TEM analyses were performed with a Philips CM200 Field Emission Gun (FEG) instrument operating at 200 kV using A CCD camera. Images were collected on SO-163 film and digitized using a Minolta DiMAGE scanner at 2400 dpi resolution. Composites were ultramicrotomed with a RMC PowerTome XL to the thickness of (50–70) nm at room temperature using a 45° diamond knife with a 6° clearance angle. Cryomicrographs were taken after placing a droplet of oxidized PR-19-PS/D_2O dispersion on a copper grid and instantly cooling to liquid nitrogen temperature.

### 2.2.4. Dynamic mechanical thermal analysis (DMTA)

The dynamic storage modulus (E') and loss factor ($\tan\delta$) were determined by DMTA, performed in bending mode versus temperature 25–300 °C at a heating rate of 2 °C per min) using a Polymer Laboratories DMTA MK III instrument. A dual cantilever beam bending mode was employed. Small amplitude bending oscillations (10 Hz) were used at a gap setting of 8.00 mm. The test samples were approximately 3.0–4.0 mm thick, 4.5–5.5 mm wide, and 38 mm long.

3. Results and discussion

3.1. Carbon nanofiber characterization

PR-19-HT and PR-19-PS (after a 12 h treatment in 70% by weight HNO_3 at 115 °C) exhibit a bamboo type structure and

Fig. 2 – Schematic representation of the hollow cylinder model.
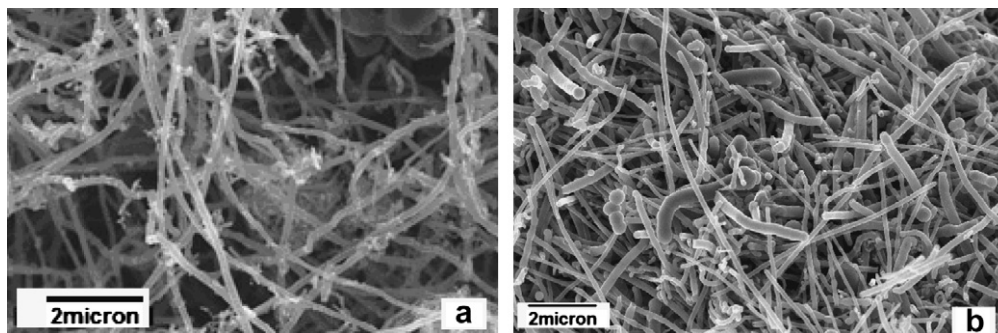
Fig. 3 – Typical SEM electron micrographs of dry CNF: (a) PR-19-HT carbon nanofibers and (b) Nitric acid-oxidized PR-19-PS carbon nanofibers.

some show a conical head (Fig. 3a and b). Their surfaces appear to be smooth and most fibers are hollow with diameters ranging from 60 to 200 nm and lengths of several hundred nanometers to many microns. The fibers form clusters of small nested balls in their dry state. Nested aggregates range from 1 to 2 μm to 100 μm in diameter in as-received samples prior to dispersion. PR-19-HT shows less polydispersity in both diameter and length, perhaps a result of the high temperature treatments and more highly graphitized structure. Oxidized PR-19-PS fibers have larger thicknesses and a few appear to be solid cylinders and not hollow tubes. The average diameters of PR-19-HT and oxidized PR-19-PS were 84 ± 3 nm and 164 ± 7 nm, respectively (determined by SEM averaged over 150 individual fibers in each case). Both samples exhibit large diameter polydispersities.

3.1.1. Carbon nanofiber in D_2O

Dilute dispersions (0.025 volume fraction) of PR-19-HT and oxidized PR-19-PS in D_2O were studied by SANS and cryo-TEM to determine the fiber dimensions. PR-19HT carbon nanofibers in D_2O precipitated due to the poor interaction between graphitic carbons and polar water molecules. The precipitation of oxidized PR-19-PS in D_2O occurred far more slowly because of hydrophilic interactions between

oxygenated functional groups (–COOH, –OH, quinoid, anhydride and ether groups) present at the surface of oxidized CNF. This higher dispersion stability allowed small angle neutron scattering experiments to be performed on the D_2O dispersion.

Cryo-TEM examination of 0.025 volume fraction oxidized PR-19-PS/D_2O dispersion exhibited predominantly single fibers (Fig. 4a). Micrographs were taken while the ice was constantly subliming upon a few minutes of exposure to the electron beam. A very small fraction of fibers interacted with other fibers (Fig. 4b). Observed fibers did not exhibit as much bending and curvature in the frozen state as appeared in the as-received dry fiber or the dried fiber after nitric acid oxidation. The internal structures of the hollow fibers appear to be filled with ice. This interesting observation may suggest that oxygenated functions possibly exist on the inside surfaces of the hollow tube fibers. The high aspect ratios of these tubes would make it very difficult for water to penetrate throughout the longitudinal axis if these inner surfaces were hydrophobic. The radii of the oxidized PR-19-PS CNF in micrograph 4a and 4b are in the range (55–142) nm and the fiber wall thicknesses are (25–74) nm. These values are measurements only from fibers in the micrographs Fig. 4a and b and are not averaged values over a large number.
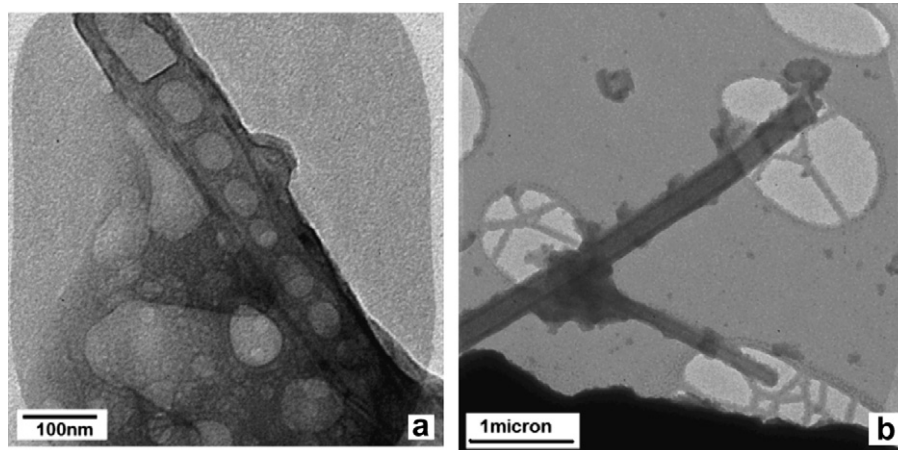
Fig. 4 – Cryo-TEM imaging of the dispersed nanofibers in D_2O showed predominantly isolated fibers with a small fraction of the aggregates: (a) Isolated oxidized PR-19-PS in ice with infusion of ice inside oxidized PR-19-PS and (b) CNF in ice with fiber–fiber interactions. Nitric acid-oxidized PR-19-PS fibers show little bending or curvature in the frozen state.
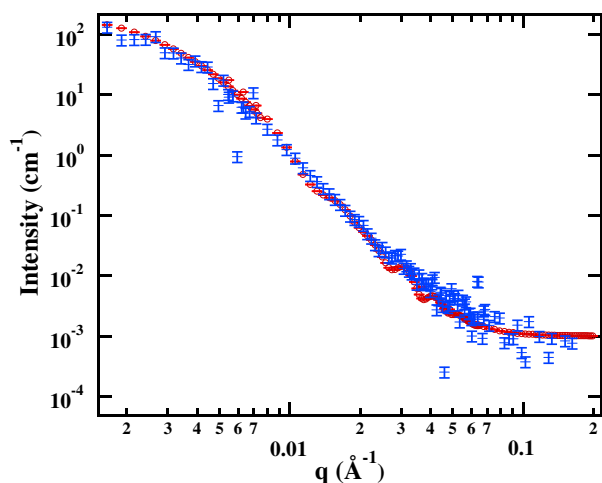
Fig. 5 – Comparison of the polydisperse hollow cylinder model (red, ○) with the experimental scattering data from oxidized PR-19-PS in D_2O (blue, +). (For interpretation of the references in colour in this figure legend, the reader is referred to the web version of this article.)

3.1.2. SANS of CNF in D_2O

The scattered intensity versus q of the oxidized PR-19-PS dispersion (0.025 volume fraction of CNF) in D_2O shows a plateau in the low q region (Fig. 5), indicating the presence of non-interacting scatterers in solution within the examined q range. This agrees with predominantly isolated oxidized PR-19-PS fibers within examined q range and length scales [30]. Applying the Guinier approximation (Eq. (6)) leads to an I_0 of 141.2 1/cm and $R_g = 54$ nm.

Scattering data from the oxidized PR-19-PS fibers in D_2O is approximated by the polydisperse hollow cylinder form factor model (Eq. 3, Fig. 5). Comparing the polydisperse hollow cylinder model with the scattering data gives a mean fiber radius of 75.5 nm, a shell thickness of 56 nm, and a fiber core radius of 19.5 nm and radial polydispersity of 0.96 when the scattering contrast is $3.3e{-}7\,\text{Å}^{-2}$ (scattering length density of C $6.66e{-}6\,\text{Å}^{-2}$) (Table 1). The model was not very sensitive to the fiber length and a range of length 60–150 nm with the best fit value of 69 nm was predicted by the model. The fiber lengths obtained by cryo-TEM are in the range of microns which is not in agreement with this model prediction.

Table 1 – Physical properties of materials

Material	Molecular mass (g)	Density (g/cm^3)	Neutron scattering length density[a] (SLD) (Å^{-2})
C	12.01	2.0	6.66×10^{-6}
D_2O	20.03	1.1	6.33×10^{-6}
Phenolic resin, $(C_6H_4O_3)_n$	124.1	0.9	1.85×10^{-6}

a Calculated from the formula: $SLD = \sum b_{ci}/v_m$, (b^{ci} is the bound coherent scattering length of ith of a molecule and v^m is the molecular volume (http://www.ncnr.nist.gov/resources/sldcalc.html).
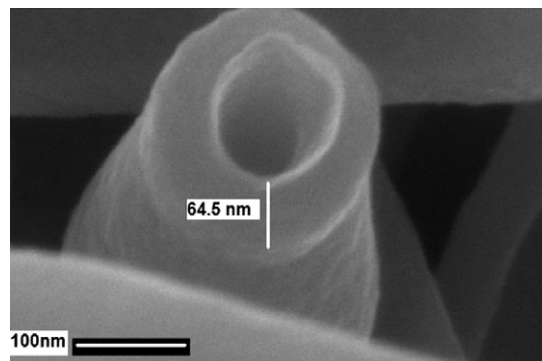
Fig. 6 – SEM micrograph of PR-19-PS in dry state illustrates CNF in three-dimensions.

Although the neutron scattering contrast is small, D_2O (SLD: $6.33e{-}6\,\text{Å}^{-2}$) was used in preference to H_2O (SLD: $-5.6e{-}7$) to reduce the incoherent scattering. The contrast was sufficient to result detectable scattering intensity for dilute dispersions of CNF. The small contrast between CNF and D_2O results in minimal scattering from the core (a cylinder model can predict the same fiber radius). The mathematical expression of the hollow cylinder can be simplified to the cylinder form factor if the scattering contrast between core and fiber is negligible. The fiber radius predicted by the models (75.5 nm) is in the range of cryo-TEM observation (55–142) nm. The fiber shell thickness to fiber radius ratio predicted by the hollow tube model is 0.74 versus 0.45–0.52 observed in cryo-TEM micrographs. Fig. 6 exhibits a three-dimensional structure of oxidized PR-19-PS. The fiber radius, shell thickness, core radius and polydispersity obtained in this analysis should not be compared with the fiber characteristics in the phenolic resin because fibers were partially precipitated in D_2O. Data analysis is only reproducible for the exact concentration of the oxidized PR-19-PS (with the same fiber size range) when characterized in the neutron beam at the same wave length (and dispersion), beam flux and acquisition time. Any change in these parameters will vary the data.

Scattering from this oxidized PR-19-PS/D_2O suspension exhibits a power law slope of $\sim$$-3.8$ in the medium q range. A power law slope of -4 indicates a sharp interface between two phases while a power law slope of -3 has been attributed to the presence of three-dimensional fractal objects [28–31].

3.2. Composite properties

3.2.1. Thermal and mechanical properties of composites

Figs. 7 and 8 illustrate the dynamic thermal mechanical (DMA) data of the PR-19-HT carbon nanofiber phenolic resin composites. The composite's storage bending modulus increased modestly at temperatures below T_g with PR-19-HT fibers. However, this modulus increased greatly at temperatures above T_g as the CNF content in the resin was raised. This is consistent with reported DMA results from epoxy/carbon nanofiber composites [33]. Oxidized PR-19-PS fiber/phenolic resin composites gave the same trend. CNFs have very high modulus that changes minimally with increasing temperature. CNF reinforcement results in high storage bending
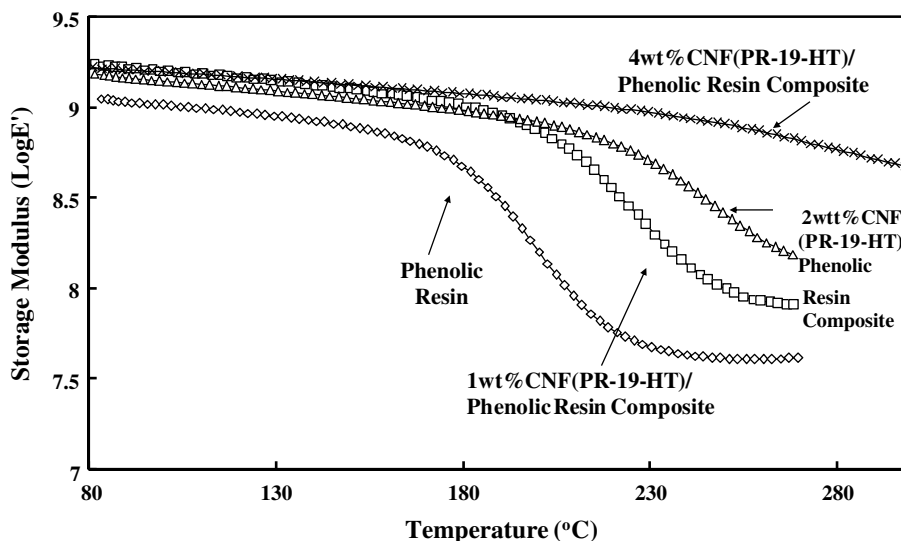
Fig. 7 – Storage bending modulus of PR-19-HT phenolic resin composites at 10 Hz. With the addition of CNF, there is a modest increase of the modulus below T_g. Above T_g, there is a large increase in the elastic bending modulus that is larger as the concentration of CNFs is increased.
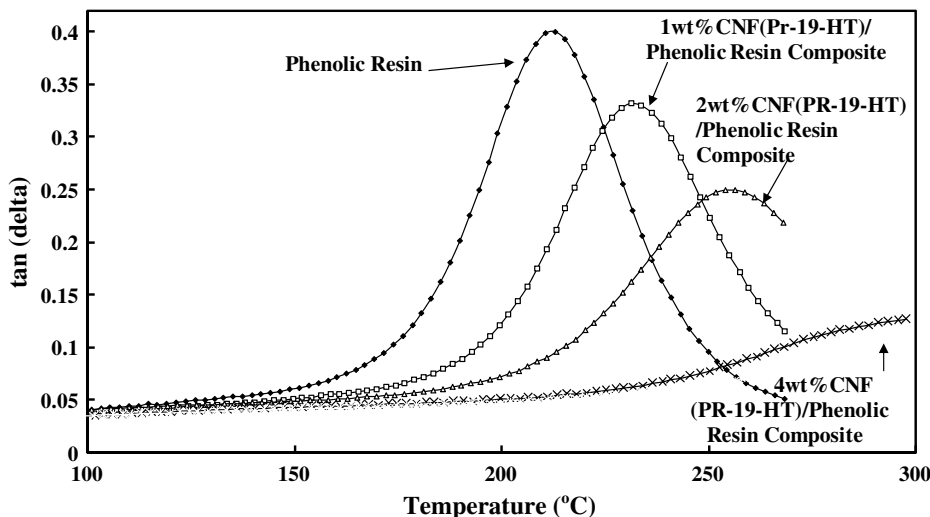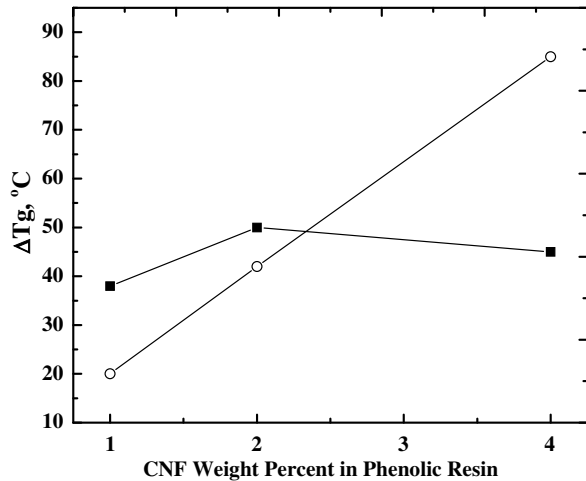

Fig. 8 – tan δ of 1%, 2%, and 4% by weight PR-19-HT/phenolic resin composites.

modulus of CNF/phenolic resin composites at elevated temperatures, allowing their application at higher temperatures.
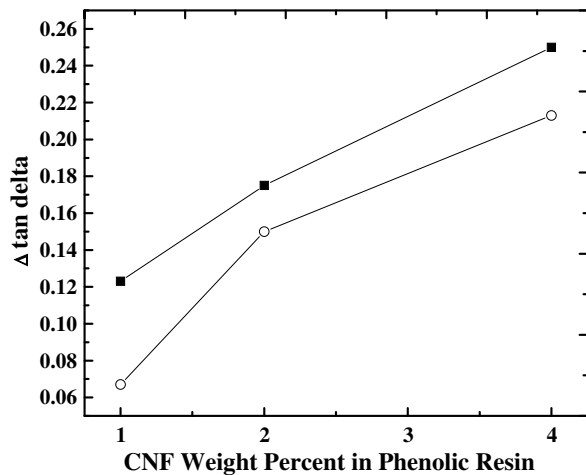
Fig. 9 illustrates the T_g increase ($\Delta T_g = T_{g\ composite} - T_{g\ cured\ phenolic\ resin}$) when either PR-19HT or oxidized PR-19PS nanofibers were incorporated into the phenolic composites. T_g values increased for both composite series up to 4% by weight CNF loading. Further increases in the CNF loading resulted in a T_g decrease. Enhanced T_gs have been reported previously for high CNF loadings in CNF/epoxy resin composites [33]. The T_g enhancement was more prominent for surface-oxidized PR-19-PS/phenolic resin versus PR-19-HT/phenolic resin composites both at 1% and 2% by weight CNF loadings. T_g increased linearly with an increase in loading for PR-19-HT composites with up to 4% by weight CNF. However, the signif-

icant T_g increase for 1% and 2% by weight PR-19-PS samples did not continue upon raising the CNF loading to 4% by weight. The T_g of the 4% by weight composite was slightly lower than that of its 2% analogue, but absolute T_g remained higher than that of the pure phenolic resin.

The CNF surfaces restrict adjacent polymer chain segmental motions if physical or chemical interactions between the polymer and the CNF surface exist. Resin species with hydroxyl functionality can be adsorbed on CNF surfaces with oxygenated functional groups. Hydrogen-bonding and, after curing, chemical resin-to-fiber bonding can restrict adjacent polymer segments mobility. Therefore, CNF present in cured phenolic resins have a significant influence on the composite properties. The large nanofiber surface area per unit weight

Fig. 9 – The increase in glass transition temperature of the cured resole phenolic resin (Hitco 134A) upon incorporation of oxidized PR-19-HT (○) and PR-19-PS (■) nanofibers. T_g increase is plotted as $\Delta T_g = T_{g\ composite} - T_{g\ phenolic\ resin}$ versus CNF weight percentage.

Fig. 10 – Decrease in the magnitude of the maximum $\tan\delta$ ($\tan\delta = E'/E''$) values upon incorporation of PR-19-HT (○) and PR-19-PS (■) nanofibers. The decrease in $\tan\delta$ ($\Delta\tan\delta = \tan\delta_{cured\ phenolic\ resin} - \tan\delta_{composite}$) is plotted versus CNF weight percentage.

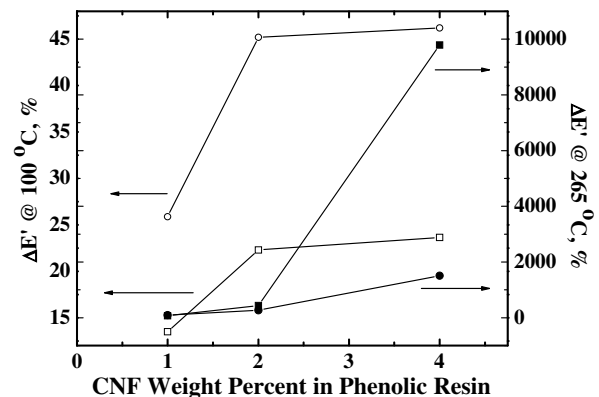emphasizes the importance of the interfacial region's properties on the composite properties.

The decrease in the magnitudes of the maximum $\tan\delta$ values for the composites versus that of the pure cured phenolic resin ($\Delta\tan\delta = \tan\delta_{phenolic\ resin} - \tan\delta_{composite}$) is plotted versus CNF loading (Fig. 10). The maximum value of $\tan\delta$ ($\tan\delta = E'/E''$) decreases with increasing CNF content. Furthermore, the absolute value of this magnitude change (e.g. $\Delta\tan\delta$) is increasing. This increase in $\Delta\tan\delta$ is more significant for the oxidized PR-19-PS/phenolic resin composites. This observed damping reduction shows that CNF addition is making the composite more elastic and less viscous. The

stronger fiber-to-resin interactions of the surface-oxidized fibers cause a larger damping reduction. These effects are remarkably large for such small fiber weight fractions. Furthermore, the fiber volume fractions are about one half of their weight fractions because the fiber density is about twice that of the phenolic resin. This emphasizes that large property changes are induced by small concentrations of nanofibers.

The $\tan\delta$ peaks broaden with increasing CNF content, indicating the presence of a broad range of polymer segment relaxation times. These $\tan\delta$ curves are progressively displaced to higher temperature with more CNF content. Increasing crosslinking density could contribute to increase in T_g and modulus. Assuming similar degrees of polycondensation and crosslinking, this trend can be attributed to decreased segmental freedom due to fiber–resin interactions in the interfacial regions. As CNF loading increases, interfacial regions constitute an increasing volume fraction.

The bending storage moduli increase with CNF addition. Fig. 11 illustrates the percentage increase in composite modulus upon the addition of 1–4% by weight of oxidized PR-19-PS or PR-19HT fibers. The bending storage modulus, E', for both composite series exhibited modest enhancements with added CNF below T_g, ranging from 13.5% to 23.7% and 25.9% to 46.2% for oxidized PR-19-PS/phenolic and PR-19-HT/phenolic composites, respectively. In contrast, much larger increases in the bending storage modulus were observed above the glass transition temperature. A similar trend has been reported for storage bending modulus of CNF/epoxy resin composites [33].
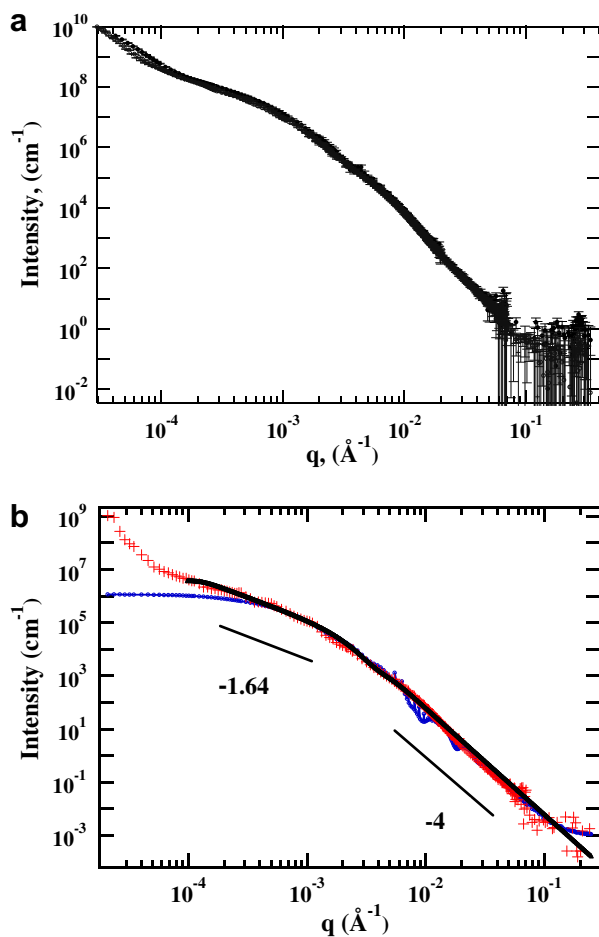
These remarkable enhancements above the T_g do not fit any standard rule of mixtures or other straightforward analysis. The larger increase of the modulus of the oxidized PR-19-PS containing composites could be due to better fiber–resin adhesion, covalent bonding of the fiber to phenolic resin and improved fiber dispersion.
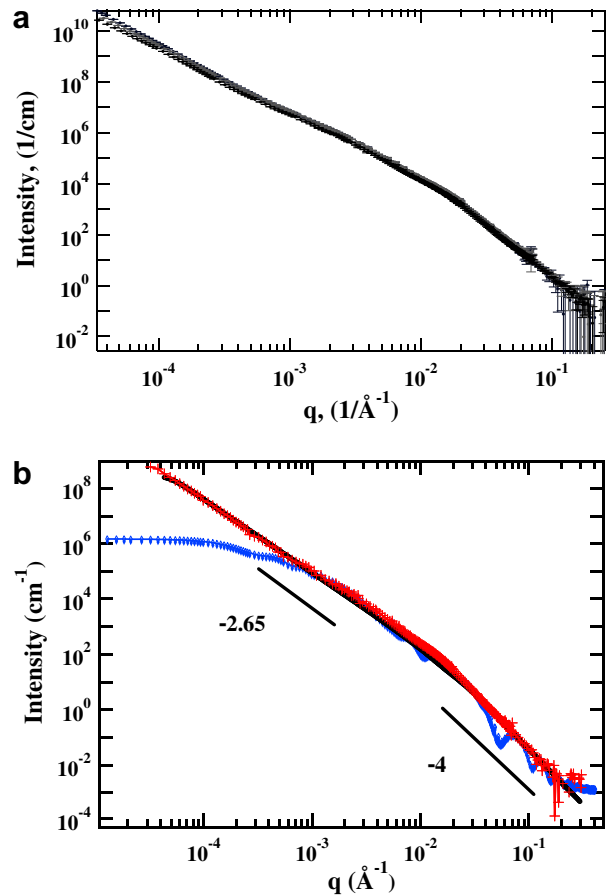

Fig. 11 – Increase of the bending storage modulus of the composites ($\Delta E'$, expressed as percent) versus that of the cured phenolic resin ($\Delta E' = \Delta E'_{composite} - \Delta E'_{cured\ phenolic\ resin}$) at 100 °C (below T_g) and at 265 °C (above T_g) plotted versus CNF weight percentage. The symbols are PR-19-HT (○) and PR-19PS (□) for $\Delta E'$ at 100 °C and PR-19-HT (●) and PR-19PS (■) for $\Delta E'$ at 265 °C.

3.2.2. SANS of CNF/phenolic resin composites

Previous studies in our laboratories have shown no thermal and mechanical property enhancement when large fiber aggregates and nesting exist. Properties can deteriorate. Therefore, it is crucial to understand the fiber structure and dispersion in the cured composites where properties were improved. Fiber dimensions and the degree of dispersion in the composites were elucidated by neutron scattering and electron microscopy to correlate with properties. Scattering intensities of 1–4% by weight oxidized PR-19-PS, or 1–4% by weight PR-19-HT composites were normalized versus volume fraction after subtraction of the incoherent background. This resulted in one normalized curve, confirming that both morphological parameters and CNF dispersion in phenolic resin
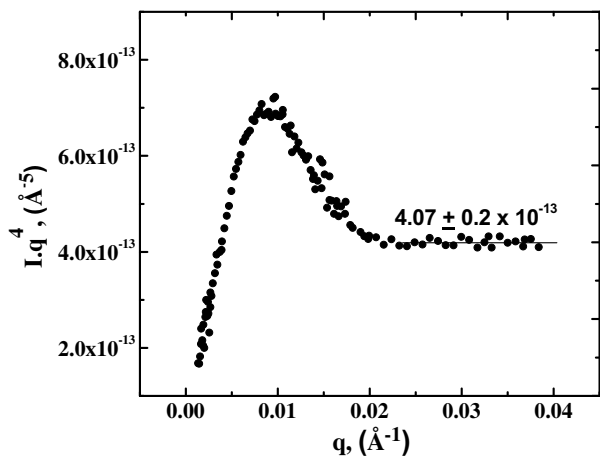
Fig. 13 – (a) Scattered intensity versus q of PR-19-HT/ phenolic resin composites, normalized with respect to volume fraction (ϕ = 0.00553, 0.0111, 0.0224), (b) Theoretical representation of the polydisperse hollow cylinder model (blue, ○), the experimental SANS data of PR-19-HT/phenolic resin, ϕ = 0.0224, (red, **+**) and the theoretical representation of the unified model (black, Δ) are plotted. The oscillation of the polydisperse hollow cylinder model in the medium q range is due to monodisperse fiber lengths and thicknesses in the model calculation. (For interpretation of the references in colour in this figure legend, the reader is referred to the web version of this article.)

Fig. 12 – (a) Scattered intensity versus q of oxidized PR-19-HT/phenolic resin composites, normalized with respect to volume fraction (ϕ = 0.00553, 0.0111, 0.0224), (b) Theoretical representation of the polydisperse hollow cylinder model (blue, ○), experimental SANS data of oxidized PR-19-PS/phenolic resin, ϕ = 0.011, (red, **+**), and theoretical representation of the unified model (black, Δ) are plotted. The oscillation of the polydisperse hollow cylinder model in the medium q range is due to monodisperse fiber lengths and thicknesses in the model calculation. (For interpretation of the references in colour in this figure legend, the reader is referred to the web version of this article.)

were independent of CNF loadings up to 4% by weight fiber within the examined q-range (Fig. 12a and 13a). Although the CNFs are microns long, the fiber–fiber interactions do not have any influence on the scattering features in the q-range that was measured. Therefore, only one set of scattering data was analyzed for each series of the three composites to quantify the fibers form factor.

The experimental scattering data from the oxidized PR-19-PS and PR-19-HT phenolic composites (with incoherent background subtracted) were compared with a polydisperse hollow cylinder model (Fig. 12b and 13b). The difference between scattering length density (SLD) of carbon, 6.66×10^{-6} Å^{-2}, and that of the phenolic resin, $1.85e-6$ Å^{-2} was 4.81×10^{-6} Å^{-2}. The SLD of phenolic resin were calculated from the density of phenolic resin (0.9 g/cm^3). Its atomic

Fig. 14 – The SANS data from oxidized PR-19-PS/phenolic resin composites plotted as $I \cdot q^4$ versus q, where I is the normalized scattering intensity with respect to fiber volume fraction. The plateau value is proportional to the specific surface area, S/V.

The S/V for a hollow cylinder is $2/(r_0 - r_i)$ from which an average value for the fiber shell thickness can be found. These fiber shell thickness averages were 71.5 and 12 nm for oxidized PR-19-PS and PR-19-HT fibers, respectively. The smaller average PR-19-HT thickness results from high temperature fiber treatment that enhances crystallinity, density, and graphitization. Fig. 15a exhibits the cross section of CNF in phenolic resin (Fig. 15a) where the fiber with the bamboo structure is filled with phenolic resin. Fig. 15b illustrates the graphitic planes composing the CNF cross sections.

The shell thickness values from Porod analysis were used as known values in the polydisperse hollow cylinder model. The SLD of the phenolic resin was used for the inner volume of the hollow cylinder. Only carbon nanofiber form factor contributions to the scattering data were considered. The polydisperse hollow cylinder model with a face thickness was used to predict oxidized PR-19-PS structural parameters in the cured phenolic composites (Fig. 12b). A radial polydispersity of 0.94, a face thickness of 6.5 nm, a mean core radius of 38.5 nm and an average fiber length of 2.4 μm for the $q > 3.1 \times 10^{-4}$ Å^{-1}, when employing the known carbon nanofiber volume fraction, scattering length density and fiber shell thickness were predicted. The model's minimum accuracy for fiber length is ±50 nm. The large size of fibers precludes accurate model prediction. The theoretical model exhibits oscillations for $q > 0.00571$ 1/Å, due to the use of monodisperse fiber lengths and shell thickness in the theoretical model. The low q upturn is most likely due to the presence of loose fiber networks within the resin.

The experimental scattered intensity of the 1%, 2%, and 4% by weight PR-19-HT composites, normalized with respect to volume fraction, are compared with the polydisperse hollow cylinder model (Fig. 13b). The fiber shell thicknesses obtained from Porod analysis and the scattering length densities were used as known values for input into the model. This model predicted a PR-19-HT fiber core radius of 32 nm, a radial polydispersity of 0.83, a face thickness of 8.5 nm and an average length of 1.55 μm for $q > 8.2 \times 10^{-4}$ Å^{-1} (Table 2). Since, the model is not sensitive to large values of fiber length, it can

composition was obtained from elemental analysis (Table 1). The experimental scattering data from the three fiber loadings in each of the two CNF composite series exhibit a Porod scattering with a power law slope of -4 when $q > 0.01$ 1/Å. This confirms the presence of a sharp carbon nanofibers and matrix resin interface [30–32]. The interfacial areas were found from the limiting values of $I \cdot q^4$ versus q plots (Fig. 14).
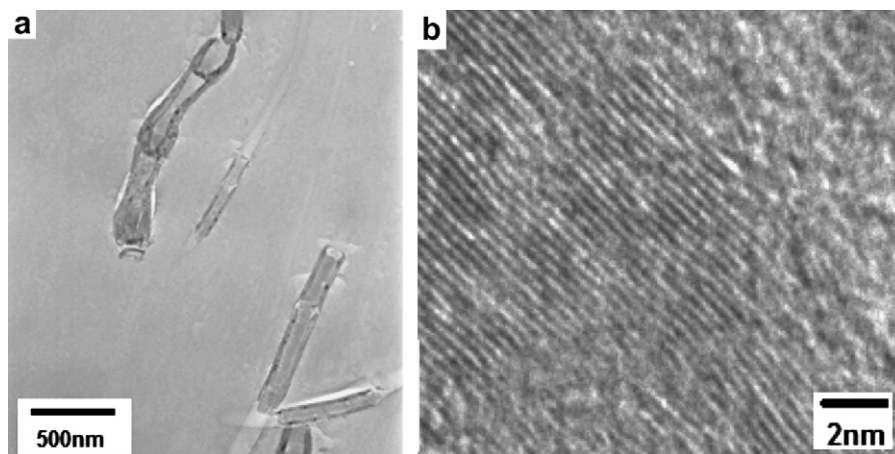
$$\lim_{q \to \infty} I \cdot q^4 = 2\pi\Delta\rho^2 \left(\frac{S}{V}\right) \qquad (8)$$

The limiting value is proportional to the ratio of the surface area to volume (S/V) and square of the contrast (difference between scattering length densities). The calculated S/V ratios for PR-19-HT and oxidized PR-19-PS fibers in the cured phenolic resins are 0.0167 and 0.0028 Å^2/Å^3, respectively. The larger diameter fiber, oxidized PR-19-PS, has the smaller S/V value.

Fig. 15 – Bright field, high-resolution transmission electron micrographs showing, (a) bamboo structured and cylindrical hollow carbon nanofibers (oxidized PR-19-PS) within the cured phenolic resin, (b) cross sections of oxidized PR-19-PS illustrating graphitic planes with turbostratic partially amorphous carbon appearing on the outer surface (upper right corner).

Table 2 – Carbon nanofiber dimensions in phenolic resin composites, in D_2O and as-received determined from SEM and SANS

	Carbon nanofibers		
SEM	PR-19-HT		Oxidized PR-19-PS
Average fiber radius (nm)	42		82
SANS			
Porod analysis			
Average surface to volume ratio (Å^2/Å^3)	0.0167		0.0028
Shell thickness (nm)	12		71.5
Polydisperse hollow tube model	CNF in phenolic resin		CNF in D_2O
	PR-19-HT	Oxidized PR-19-PS	Oxidized PR-19-PS
Average core fiber radius[a] (nm)	32	38.5	19.5
Average shell thickness[a] (nm)	12	71.5	56
Average fiber radius[a] (nm)	44	110	75.5
Polydispersity	0.83	0.94	0.96
Fiber length[b] (μm)	1.55	2.44	0.69

a The error in the reported radii values are less than ±0.5 nm.
b The error in the reported lengths are minimum ±50 nm.

only predict lengths with a minimum accuracy of ±50 nm. We know fiber lengths above 10 μm are present in the as-received fibers so the length results from this treatment are not good estimates of the real length distributions. Sonication, crushing and grinding during composite fabrication may lower the average fiber length via fiber breaking. Thus, it is difficult to estimate the accuracy of establishing fiber lengths by this method. The fiber lengths exceed the size scales suitable for characterizations by SANS and USANS. Oscillation of the theoretical model is due to the use of monodisperse fiber length and shell thickness and aggregation which starts at $q > 1.73 \times 10^{-2}$ Å^{-1} for PR-19-HT.

Fiber diameters predicted from SANS data by the polydisperse hollow cylinder model (220 nm for PR-19-PS and 88 nm for PR-19-HT) are somewhat larger than those observed in SEM micrographs (164 and 84 nm, respectively). The standard deviations of the Gaussian distributions for fiber core radii were 0.94 and 0.83, indicating high fiber core radius polydispersity. The average oxidized PR-19-PS fiber length predicted within the resin (2.4 μm) is larger than that of the PR-19HT fibers (1.55 μm). This was expected based on the known larger PR-19-PS dimensions observed in SEM (Table 2).

The Beaucage unified model is compared to the experimental data from both the PR-19-HT and oxidized PR-19-PS composites (Fig. 12b and 13b). The unified model prediction for the quasi power law slope of the PR-19-HT fiber composites is $P = 2.65$, $q^{-2.65}$, in the range of $q < 0.01561$ 1/Å (Table 3). The Guinier radius of gyration R_g predicted for this q range is 7.8 μm. Predicted values for the oxidized PR-19-PS/resin composites are $P = 1.64$ for $q < 0.00165$ 1/Å and $R_g = 2.89$ μm. The smaller R_g value and smaller absolute value of the power law slope (1.64) for oxidized PR-19-PS suggest a looser fiber network and improved dispersion. Better dispersion is expected because the carboxylic, phenolic hydroxyl, and quinoids functions on the fibers promote resin/fiber compatibility. The high q quasi power law slope was −4 for both PR-19-HT and oxidized PR-19-PS composites.

3.2.3. TEM of CNF phenolic resin composites

Nanofiber dispersions in the PR-19-PS and PR-19HT phenolic resin composites were examined using TEM (Fig. 16a and b). Fiber bundles and aggregates were more evident in the PR-19-HT composites, even at low loading levels. Composites with oxidized PR-19-PS fibers exhibited improved dispersion with larger fiber/fiber distances. This is consistent with the smaller radius of gyration (2.89 μm for PR-19-PS versus 7.89 μm for PR-19-HT fibers) predicted by the Unified Beaucage model and a quasi power law slope of −1.64 for PR-19-PS (versus −2.65 for PR-19-HT). Some loose fiber bundles and aggregates still exist in the oxidized PR-19-PS composites. PR-19-HT carbon nanofibers exhibit nesting with some infusion of phenolic resin into these aggregates.

Table 3 – Carbon nanofiber dispersion in phenolic resin composites predicted by unified model

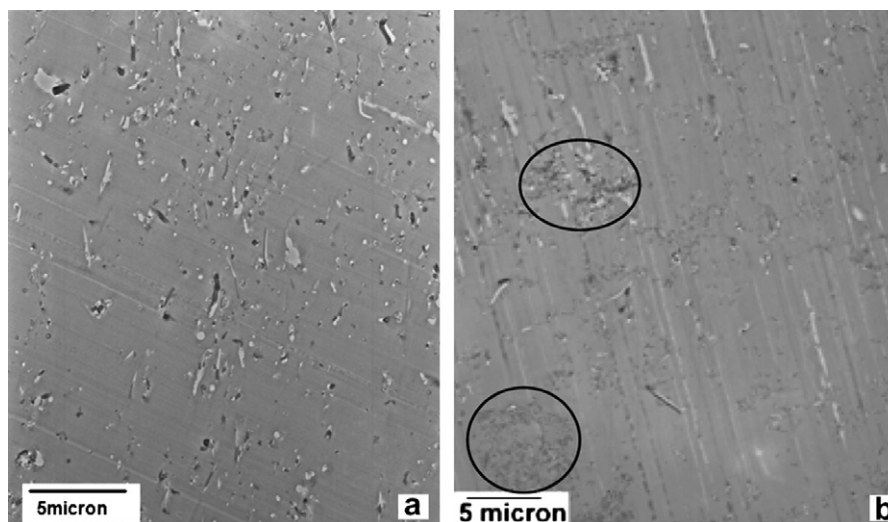|	Low q			High q	
	PR-19-HT	Oxidized PR-19-PS		PR-19-HT	Oxidized PR-19-PS
Unified Beaucage model					
R_{g1} (μm)	7.89	2.89	R_{g2} (μm)	0.0162	0.076
Power	2.65	1.64	Power	4	4
B (cm^{-1} sr^{-1})	0.0008	0.79	B (cm^{-1} sr^{-1})	3e−6	3.4e−7
G (cm^{-1} sr^{-1})	115	102	G (cm^{-1} sr^{-1})	135	850

Fig. 16 – Transmission electron micrographs of (a) 4% by weight oxidized PR-19-PS/phenolic resin and, (b) 4% by weight PR-19HT/phenolic resin composites. Circled areas in micrograph (b) denote the CNF aggregates.

4. Conclusions

Nitric acid-oxidized PR-19-PS and unoxidized PR-19-HT carbon nanofiber composites exhibited increased glass transition temperatures and substantially higher dynamic bending modulus at temperatures above T_g versus the neat cured phenolic resin. Oxygenated surface functions produced by nitric acid oxidation improved both fiber/water and fiber/phenolic resin compatibility. Water suspensions of oxidized CNFs settled much slower than unoxidized CNFs. The CNF dispersion and the morphological parameters in the resin were independent of fiber loading between 1% and 4% by weight. Analysis of SANS and USANS data from PR-19-HT and oxidized PR-19-PS composites and by the polydisperse hollow tube model provided the average fiber core radii, average fiber diameters, radial polydispersities and fiber lengths *in-situ*. Both PR-19-HT and oxidized PR-19-PS composites exhibited a Porod scattering with a power law slope of -4, indicating the presence of sharp fiber/phenolic resin interfaces. The radii of gyration and power law slopes were obtained from the unified Beaucage model. The smaller radius of gyration and a power law slope of -1.64 for oxidized PR-19-PS in phenolic resin agree with the dispersion results obtained from TEM.

Acknowledgements

REFERENCES

[1] Koyama T. Formation of carbon fibers from benzene. Carbon 1972;10:757–8.
[2] Koyama T, Endo M. Structure and growth processes of vapor-grown carbon fibers. Ohyo Butsuri 1973;42:690–5 [in Japanese].
[3] Chung DDL. Comparison of submicron-diameter carbon filaments and conventional carbon fibers as fillers in composite materials. Carbon 2001;39:1119–25.
[4] Brandl W, Marginean G, Chirilia V, Warschewski W. Production and characterisation of vapour grown carbon fiber/polypropylene composites. Carbon 2004;42:5–9.
[5] Koerner H, Vaia RA, Liu W, Alexander M, Mirau P. Deformation–morphology correlations in electrically conductive carbon nanotube—thermoplastic polyurethane nanocomposites. Polymer 2005;46:4405–20.
[6] Koerner H, Price G, Pearce NA, Alexander M, Vaia RA. Remotely actuated polymer nanocomposites–stress-recovery of carbon-nanotube-filled thermoplastic elastomers. Nat Mater 2004;3:115–20.
[7] Kumar S, Dang TD, Arnold FE, Bhattacharyya AR, Min BG, Zhang X, et al. Synthesis, structure, and properties of PBO/SWNT composites. Macromolecules 2002;35:9039–43.
[8] Velasco-Santos C, Martinez-Hernandez AL, Fisher FT, Ruoff R, Castano VM. Improvement of thermal and mechanical properties of carbon nanotube composites through chemical functionalization. Chem Mater 2003;15:4470–5.
[9] Xu J, Donohoe JP, Pittman Jr CU. Preparation, electrical and mechanical properties of vapor grown carbon fiber (VGCF)/vinyl ester composites. Compos Part A 2004;35:693–701.
[10] Jang J, Bae J, Choi M, Yoon SH. Fabrication and characterization of polyaniline coated carbon nanofiber for supercapacitor. Carbon 2005;43:2730–6.

[11] Tibbetts GG, Doll GL, Gorkiewicz DW, Moleski JJ, Perry TA, Dasch CJ, et al. Physical properties of vapor-grown carbon fibers. Carbon 1993;31:1039–47.

[12] Boudou JP, Martinez-Alomzo A, Tascon JMD. Introduction of acidic groups at the surface of activated carbon by microwave-induced oxygen plasma at low pressure. Carbon 2000;38:1021–9.

[13] Patton RD, Pittman Jr CU, Wang L, Hill JR, Day A. Ablation, mechanical and thermal conductivity properties of vapor grown carbon fiber/phenolic matrix composites. Compos Part A 2002;33:243–51.

[14] Blanski R, Koo JH, Ruth P, Nguyen H, Pittman Jr CU. Polymer nanostructured materials for rocket motor insulation – ablation performance. In: Proceeding meeting, 52nd JANNAF, Las Vegas, NV: Porpulsion meeting; 2004. p. 1–18.

[15] Pittman Jr CU, Blanski RL, Phillips SH, Koo JH, Ruth PN. Rocket motor insulation. US patent, AF invention no AFB00685; 1995.

[16] Trick KA, Saliba TE. Mechanisms of the pyrolysis of phenolic resin in a carbon/phenolic composite. Carbon 1995;33:1509–15.

[17] Montes-Morán MA, Martínez-Alonso A, Tascón JMD, Paiva MC, Bernardo CA. Effects of plasma oxidation on the surface and interfacial properties of carbon fibres/polycarbonate composites. Carbon 2001;31:1057–68.

[18] He P, Gao Y, Lian J, Wang L, Qian D, Zhao J, et al. Surface modification and ultrasonication effect on the mechanical properties of carbon nanofiber/polycarbonate composites. Compos Part A 2006;37:1270–5.

[19] Shi D, Lian J, Peng H, Wang LM, Xiao F, Yang L, et al. Plasma coating of carbon nanofibers for enhanced dispersion and interfacial bonding in polymer composites. Appl Phys Lett 2003;83:5301–3.

[20] Lakshminarayanan PV, Toghiani H, Pittman Jr CU. Nitric acid oxidation of vapor grown carbon nanofibers. Carbon 2004;42:2433–42.

[21] Zhao J, Schaefer DW, Shi D, Lian J, Brown J, Beaucage G, et al. J Phys Chem B 2005;109:23351.

[22] Tibbetts GG, Endo M, Beetz Jr CP. Carbon fibers grown from the vapor phase: a novel material. SAMPE J 1986;22: 30–5.

[23] Tibbetts GG, Beetz Jr CP. Mechanical properties of vapor-grown carbon fibers. J Phys D: Appl Phys 1987;20:292–7.

[24] Oberlin A, Endo M, Koyama T. Filamentous growth of carbon through benzene decomposition. J Cryst Growth 1976;32:335–49.

[25] Tibbetts GG. Why are carbon filaments tubular? J Cryst Growth 1984;66:632–8.

[26] Kline SR. Reduction and analysis of SANS and USANS data using IGOR Pro. J Appl Cryst 2006;39:895–900.

[27] Agamalian M, Wignall GD, Triolo R. Optimization of a Bonse–Hart ultra-small-angle neutron scattering facility by elimination of the rocking-curve wings. J Appl Cryst 1997;30:345–52.

[28] Drews AR, Barker JG, Glinka CJ, Agamalian M. Development of a thermal-neutron double-crystal diffractometer for USANS at NIST. Physica B 1998;241–243:189–91.

[29] Higins JS, Benoit HC. Polymers and neutron scattering. Oxford: Clarendon Press; 1994. p. 15–45.

[30] Guinier A, Fournet G. Small-angle scattering of X-rays. NewYork: John Wiley and Sons; 1955. p. 22–35 and 60–75.

[31] Livsey I. Neutron scattering from concentric cylinders. Intraparticle interference function and radius of gyration. J Chem Soc Faraday Trans 2 1987;83:1445–52.

[32] Porod G. In: Glatter O, Kratky O, editors. Small-angle X-ray scattering. London: Academic Press; 1982. p. 35–45.

[33] Choi YK, Sugimoto KI, Song SM, Gotoh Y, Ohkoshi Y, Endo M. Mechanical and physical properties of epoxy composites reinforced by vapor grown carbon nanofibers. Carbon 2005;43:2199–208.